

## Growth diagram of $\text{La}_{0.7}\text{Sr}_{0.3}\text{MnO}_3$ thin films using pulsed laser deposition

Hangwen Guo,<sup>1,2</sup> Dali Sun,<sup>2,3</sup> Wenbin Wang,<sup>1,2</sup> Zheng Gai,<sup>2,4</sup> Ivan Kravchenko,<sup>4</sup> Jian Shao,<sup>5</sup> Lu Jiang,<sup>1,2</sup> Thomas Z. Ward,<sup>2</sup> Paul C. Snijders,<sup>2</sup> Lifeng Yin,<sup>5</sup> Jian Shen\*,<sup>1,5</sup> and Xiaoshan Xu\*<sup>2</sup>

<sup>1</sup>*Department of Physics and Astronomy, University of Tennessee, Knoxville, TN 37996, USA*

<sup>2</sup>*Materials Science and Technology Division, Oak Ridge National Laboratory, Oak Ridge, TN 37831, USA*

<sup>3</sup>*Department of Physics and Astronomy, University of Utah, Salt Lake City, UT 84112*

<sup>4</sup>*Center for Nanophase Materials Sciences, Oak Ridge National Laboratory, Oak Ridge, TN 37831, USA*

<sup>5</sup>*State Key Laboratory of Surface Physics and Department of Physics, Fudan University, Shanghai 200433, China*

**Abstract:** An experimental study was conducted on controlling the growth mode of  $\text{La}_{0.7}\text{Sr}_{0.3}\text{MnO}_3$  thin films on  $\text{SrTiO}_3$  substrates using pulsed laser deposition by tuning growth temperature, pressure and laser fluence. Different thin film morphology, crystallinity and stoichiometry have been observed depending on growth parameters. To understand the microscopic origin, the adatom *nucleation*, *step advance* processes and their relationship to film growth were theoretically analyzed and a growth diagram was constructed. Three boundaries

between highly and poorly crystallized growth, layer-by-layer and 3D growth, stoichiometric and non-stoichiometric growth were identified in the growth diagram. A good fit of our experimental observation with the growth diagram was found. This case study demonstrates that a more comprehensive understanding and the predicting of the growth mode in PLD is possible.

## I. INTRODUCTION

Thin film epitaxial growth using pulse laser deposition (PLD) has become one of the most popular growth techniques in condensed matter physics because of its versatility and the relatively easy ability to control certain functionalities by varying growth parameters.<sup>1-6</sup> However, the physical PLD growth process is far from simple, because it involves multiple complex steps such as ablation of target material, plasma generation and propagation through vacuum or background gas, deposition of ablated atoms on substrate, non-equilibrium processes on the surface such as diffusion, desorption, nucleation and attaching onto existing atomic steps.<sup>7-10</sup> The resulting PLD film growth mode depends strongly on all of these steps, in addition to the consideration of the cohesive energy between the ablated atoms and the binding energy between the atoms and substrate.<sup>8,9</sup> For example, it is well established that the background gas pressure plays an important role in plume collisions while acting to compensate film stoichiometry.<sup>1</sup> It is shown that a high instantaneous deposition rate implies a high supersaturation value that gives rise to a small critical nucleus and thus to a high density of nucleation sites.<sup>1,8</sup> Further, the temperature is known to have a critical influence on the diffusion barrier, which may strongly affect the growth mode. Although various kinds of growth modes

have been observed for oxide thin films under different growth conditions<sup>11-13</sup>, a growth diagram which combines multiple parameters and builds up a broad picture is still lacking.

In this work, we choose a prototypical system of  $\text{La}_{0.7}\text{Sr}_{0.3}\text{MnO}_3$  (LSMO) thin films grown on  $\text{SrTiO}_3$  (STO) (001) substrates to study the growth properties under different conditions. This doping of LSMO is a known half-metallic ferromagnet with a critical temperature above room temperature, and is of interest to many different areas, such as spin valves, resistive random access memory (RRAM), etc.<sup>14-17</sup> Theoretically, our focus is on the microscopic processes of adatom *nucleation*, *step advance* and their influence on the growth properties of oxide thin films. Based on our model analysis, we propose a growth diagram which defines the dependence of surface morphology, crystallinity and stoichiometry of oxide films on the parameters such as supersaturation and temperature. Our experimental observations of the LSMO growth modes under various growth conditions fit in the growth diagram nicely. We emphasize that the concept of supersaturation plays an important role in constructing and understanding growth diagrams for PLD thin film growth of complex oxides.

This paper is organized as follows. Section II describes the experimental conditions used in this work. Section III presents experimental results including the dependence of thin film growth properties on temperature, pressure and laser fluence. Section IV discusses the theoretically constructed growth diagram and its comparison with our experimental data.

## II. EXPERIMENTAL METHODS

Thin films of  $\text{La}_{0.7}\text{Sr}_{0.3}\text{MnO}_3$  were grown on single crystal substrates of  $\text{SrTiO}_3$  (001) (in-plane lattice mismatch of 0.8%<sup>18</sup>) using PLD with a KrF ( $\lambda = 248$  nm) laser in an oxygen background containing 10% ozone,<sup>19,20</sup> with the growth pressure of 2 mTorr. The typical film thickness is 10 nm. The repetition rate of the laser is kept at 1 Hz. *In-situ* high-pressure Reflection High Energy Electron Diffraction (RHEED) is used to monitor the entire deposition process. The time dependence of the intensity of the specular reflection was recorded. Here we employ the Pulse Laser Interval Deposition technique (see Ref. [2]), i.e. the growth periods are separated by the annealing periods (typically 5 min) in which laser pulses are paused. Specifically, the laser is paused every time when the RHEED intensity reaches a local maximum to allow sample annealing which manifests itself as the upturn of RHEED intensity. The laser pulse is resumed when the RHEED intensity saturates. The laser fluence was varied between 1 and 4 J/cm<sup>2</sup>. The substrate temperature was varied from 650 to 840 °C. The substrates are treated by buffered-HF and pre-annealed in O<sub>2</sub> (1 atm) for 3 hours at 950 °C. The target-substrate distance was 4 cm. The RHEED images were taken using KSA-400 camera at exposure time of 667 ms at the end of the growth. *Ex-situ* Atomic Force Microscopy (AFM) is used to obtain details of surface morphology. X-ray diffraction (XRD) experiments are conducted to measure the crystallinity of the films. Energy-dispersive X-ray spectroscopy (EDX) is carried out to analyze the chemical composition.

### III. EXPERIMENTAL RESULTS

#### A. Temperature dependence

We first study the influence of growth temperature while fixing the background oxygen pressure

and the laser fluence at  $1\text{J}/\text{cm}^2$ . Fig. 1a shows AFM and RHEED images of the pretreated  $\text{SrTiO}_3$  substrates. Flat surfaces with terrace width of approximately 300 nm are obtained. The sharp RHEED pattern also indicates the presence of flat terraces and a good surface crystallinity. Figure 1b and 1c show the *ex-situ* room temperature AFM, RHEED oscillations and *in-situ* RHEED images at growth temperature of  $720^\circ\text{C}$  and  $776^\circ\text{C}$ , respectively. In Fig. 1b, for the sample grown at  $720^\circ\text{C}$ , the single layer terraces inherited from the substrate are still visible while many sub-monolayer-height islands exist on top of each terrace. The RHEED intensity can only maintain its initial level for the first several oscillations, after which it decreases upon further growth. The final RHEED pattern shows weak intensity contrast, although no extra diffraction spots are present. The room temperature AFM data indicates that the growth mode is still layer by layer at  $720^\circ\text{C}$ , with a RMS roughness of only 0.14 nm. The measured X-ray Diffraction rocking curve shows the full width of half maximum (FWHM) of  $0.046^\circ$ , compared to  $0.039^\circ$  for a well-crystallized film (see supplementary material). These features suggest that the film surface is poorly crystallized with layer-by-layer feature preserved. In Fig. 1c, the room temperature AFM image of the sample grown at  $776^\circ\text{C}$  reveals neither regular terraces nor steps from the substrate and has rms roughness of 0.45 nm. The RHEED intensity decreases during the growth and displays a weak pattern with extra spots, indicating 3D island formation. For sample grown at  $840^\circ\text{C}$ , as shown in Fig. 1d, totally different features are present. Rod-like structures (as high as 100 nm) are clearly visible in the AFM image. EDX experiments were conducted to investigate the stoichiometry of these features. Fig. 1d shows the Mn-K $\alpha$  and O-K spectroscopy maps. The Mn and O concentrations of the film and the rod are different, indicating chemical

phase separation occurs in this growth regime resulting in different stoichiometry of the rods as compared to the film. As shown in Table 1, a semiquantitative analysis<sup>21</sup> indicates that the Mn:O composition ratio is roughly 1:1 on the rod and 1:3 on the film. The Sr concentration is hard to determine due to large background from the STO substrate. We cannot resolve the La concentration due to its proximity to the substrate Ti peak. According to the data in TABLE I, the composition on the rod is likely to be MnO due to the high vapor pressure of Sr and chemical bond stability of MnO.<sup>22</sup>

The temperature dependence of growth mode has also been investigated at a different laser fluence of  $4\text{J}/\text{cm}^2$ . As shown in Fig. 2a, sample grown at  $660^\circ\text{C}$  have layer-by-layer features (AFM and RHEED images will be discussed in Section II-C). The sample grown at  $760^\circ\text{C}$  shows a completely different morphology. In Fig. 2b-d, a 3D growth mode is revealed in both AFM and RHEED images. At first, the maximum intensity of primary RHEED spot gets weaker with each oscillation, then it remains nearly unchanged with almost no oscillations. The RHEED pattern shows spots with a strong intensity, indicating a well crystallized, 3D growth mode.

## B. Pressure dependence

Next, we tune the background oxygen pressure while keeping the temperature ( $730^\circ\text{C}$ ) and laser fluence ( $1\text{J}/\text{cm}^2$ ) constant. A tube was installed with its end close to the sample surface to supply an oxygen gas pressure during the growth process. To ensure the same laser and temperature conditions, we use a larger substrate ( $5\text{mm}\times 8\text{mm}$ ) and carefully position the oxygen tube nozzle with respect to the sample to create a pressure gradient over the surface of one sample. Similar approach has been used to create temperature gradient by other authors.<sup>23</sup> As shown in Fig. 3a, a

3D growth mode is obtained at low oxygen pressure, while flatter films are visible at higher pressure. In Fig. 3b, we show the rms roughness of the entire film area as measured by *ex-situ* AFM. It is clearly seen that the rms roughness decreases with the direction of increasing local pressure. To verify that the roughness distribution does not originate from temperature variations due to the large substrate size, we moved our substrate by 1 mm laterally with respect to the oxygen tube and grew a sample under the same conditions. We find that the rms roughness distribution on the sample correspondingly shifts by about 1 mm, which excludes temperature non-uniformity effects as the cause for the observed surface roughness distribution.

### C. Laser fluence dependence

In addition to the temperature and the oxygen pressure, the pulsed laser fluence is another important parameter to control the film quality. Here we keep the temperature at 740 °C and increase the laser fluence from 1 J/cm<sup>2</sup> to 2.2 J/cm<sup>2</sup>. Dramatic changes are observed in the film growth as shown in Fig. 4a and 4b. The sample grown at 1 J/cm<sup>2</sup> shows 3D features with FWHM of 0.050° in the rocking curve (see supplementary material), which indicates the poorly-crystallized nature. The sample grown at 2.2 J/cm<sup>2</sup> indicates a layer-by-layer growth mode with FWHM of 0.039°. According to Fig. 4c and 4d, perfect oscillations as well as good RHEED patterns are observed, both indicating good surface morphology and crystallinity.

### III. Discussion

As a starting point, the change in surface energy  $\Delta\sigma = \sigma + \sigma_i - \sigma_s$  is widely adopted to analyze observed surface morphology, where  $\sigma$ ,  $\sigma_s$  and  $\sigma_i$  denote the surface energy of the depositing layer, the underlying layer and the interface energy, respectively.<sup>10</sup> Indeed, such

analysis lies in the core of the origin of the well-known crystal growth mechanisms such as Volmer-Weber (VW)<sup>24</sup>, Frank-van der Merwe (FM)<sup>25</sup> and Stranski-Krastanov (SK)<sup>26</sup> growth. When  $\Delta\sigma < 0$ , layer-by-layer growth mode (FM) is favored; while 3D islands or 3D growth mode (VW) is preferred when  $\Delta\sigma > 0$ . The SK growth mode represents a transition from 2D to 3D growth when the lattice strain is taken into account. However, this description of growth is oversimplified. For example, even for  $\Delta\sigma > 0$ , it is still possible to achieve layer-by-layer growth.<sup>10</sup> As seen above, by tuning experimental parameters, different varieties of surface morphology, surface crystallinity and stoichiometry have been observed. As shown in Fig. 5a, the microscopic growth process involves multiple steps, more than the picture of surface energy change. Moreover, what also needs to be described is the relation between the growth conditions and the crystallinity and the stoichiometry of the films. Note that the discussion of stoichiometry is even beyond the picture of Fig. 5a where the smallest components are the unit cells.

The boundaries of 2D and 3D growth have been discussed in the literature. For example, Metev et al. considered the mean film thickness of a 99% covered substrate and its dependence on the growth temperature and deposition rate.<sup>1,27</sup> The boundary between a low-island growth mode and a high-island growth mode was defined in terms of the deposition rate and growth temperature. It was shown that a high deposition rate and a low growth temperature favored a 2D growth mode. By comparing the timescale of diffusion and laser pulse interval, W. Hong et al.<sup>11</sup> have constructed the boundary between step-flow growth and 2D island formation.

The crystalline properties of SrTiO<sub>3- $\delta$</sub>  homoepitaxial thin films have been reported by Ohtomo

and Hwang<sup>12</sup> The growth phase diagram in terms of O<sub>2</sub> pressure and temperature has been studied. It is noted that at the high temperature and low pressure region, the mismatching between crystallization and oxidation timescale gives rise to irregular *nucleation* and growth cycle.

In this paper, we applied the theoretical treatment in Ref. [10] on the PLD growth of oxide thin films, i.e. 1) to consider the factors of particle exchange and energy barrier in nucleation to account for the crystallization; 2) to consider the rate of *step advance* not only in terms of the diffusion process, but also the adatom concentration and their spatial gradient on the surface which all play important roles in determining the boundary between 2D and 3D growth modes. In addition, the film stoichiometry is described using the supersaturation of the corresponding vapor to solid process.

Here we first focus on the discussion on the temperature dependence of the nucleation process which strongly affects the crystallinity of thin films. Then, we focus on the discussion on the competition between *nucleation* and *step advance* (the growth of 2D islands and advance of steps), which determines the boundary of layer-by-layer and 3D growth. A growth phase diagram is developed based on those discussions in terms of growth temperature and supersaturation which is a useful concept in describing the growth conditions. Our experimental findings and theoretical model are compared to test the feasibility of our growth diagram.

#### A. Theoretical Growth Diagram

During PLD growth, the laser ablation generates a large atomic flux. As seen in Fig. 5a, these incoming atoms become adatoms on the substrate surface and diffuse. Some coalesce and

become nuclei. At low laser repetition rate,<sup>28</sup> the steady-state rate of *nucleation* can be described as (See supplementary material):

$$J_{mic} = f(\Delta\mu, T) \exp\left(-\frac{H(\Delta\mu)}{kT}\right) \quad (1)$$

$$f(\Delta\mu, T) = 2\sqrt{s_c} arN_0 \left(\frac{\Delta\mu - s_c \Delta\sigma}{\pi kT}\right)^{1/2} \quad (2)$$

$$H(\Delta\mu) = \frac{4\chi^2 s_c}{\Delta\mu - s_c \Delta\sigma} - (E_{des} - E_{sd}) \quad (3)$$

where  $s_c$  is the area of the surface unit cell;  $a$  is the lattice constant;  $N_0$  is the density of adsorption sites;  $\chi$  is the step edge energy per unit length;  $r$  is the arrival rate which is proportional to the concentration of adatoms;  $k$  is Boltzmann constant;  $E_{des}$  and  $E_{sd}$  are the desorption and diffusion energy barriers.  $\Delta\mu$ , known as supersaturation, is the chemical potential difference of adatoms transitioning from their quasi-vapor phase (the mobile adatoms on the surface and the background oxygen in the gas phase) near the substrate to their solid phase on the substrate.

The factor  $f(\Delta\mu, T)$  can be considered as an effective Zeldovich factor which accounts for the deviation of the system from the equilibrium state; it describes the rate of atom exchange between the nuclei and its quasi-vapor parent phase. The factor  $H(\Delta\mu)$  denotes the energy barrier of the *nucleation*. The competition between  $f(\Delta\mu, T)$  and  $\exp(-H(\Delta\mu)/kT)$  as a function of temperature results in a maximum value of *nucleation* rate:

$$T_{nuc}^m = H(\Delta\mu) / 2k \quad (4)$$

When the sample temperature is low, the *nucleation* rate is low because it's difficult to overcome

the *nucleation* energy barrier. At the same time, the effective Zeldovich factor is relatively high, indicating a low atom exchange rate between gas and solid. Thus, the *nucleation* rate is low and the films are not well crystallized. When the temperature is high, the *nucleation* rate is limited due to a low Zeldovich factor. However, it is easier to overcome the *nucleation* energy barrier to form nuclei. Thus, the films are well crystallized although the *nucleation* rate is also low. Consequently, Eq. (4) divides the poorly crystallized and well crystallized growth modes, as illustrated in Fig. 5b.

As shown in Fig. 5a, besides *nucleation*, another way for adatoms to contribute to the film growth is to attach to existing nuclei or steps causing *step advance*. The process includes the surface diffusion of adatoms towards the steps or edges of nuclei and incorporation of the adatoms into the kinks (See supplementary material). Assuming that the growth is in the diffusion region, i.e. the diffusion process is the limiting factor of step advance, the rate of step-advance can be written in the form of<sup>10</sup>

$$V_{sa} = 2a\nu \frac{\Delta\mu}{kT} \exp\left(-\frac{\varphi - (E_{des} - E_{sd})/2}{kT}\right) \quad (5)$$

where  $\nu$  is the vibrational frequency of the adatom;  $\varphi$  is the adsorption energy at the kink position. We note that similar to *nucleation*, the rate of step-advance is also a function of supersaturation and temperature.

The annealing process used in this work for each monolayer helps to reach layer by layer growth in the later stage of a monolayer deposition. For example, the small nucleation on top of 2D islands may become unstable due to the lowered supersaturation without laser pulses and

decompose into adatoms which eventually attach to the step edges of the lower layer via interlayer mass transfer. Thus, the processes at the early stage of a monolayer deposition such as *nucleation* and surface migration of the adatoms are more important to determine the growth properties.<sup>2</sup> In such case, the competition between the *nucleation* rate and the *step advance* rate becomes a crucial factor to determine the growth mode. As illustrated in Fig. 5c, if the *nucleation* rate  $J_{nuc}$  is much higher than the rate of *step advance*  $V_{sa}$ , new nuclei can form on top of existing islands before the completion of the underlying layer. In turn, several layers can grow simultaneously, causing 3D growth. Such a growth mode induces a reduction of the peak intensity of RHEED oscillation. In the other case, if the *nucleation* rate is much lower than the rate of *step advance*, new nuclei will form after most of the underlying layer is filled, which gives rise to a layer-by-layer growth mode.

To compare the timescales, we calculate:

$$t_{layer} = \frac{L}{V_{sa}}; \quad (6)$$

$$t_{nuc} = \frac{1}{J_{nuc} L^2} \quad (7)$$

where  $t_{layer}$  denotes the time to completely cover the substrate terrace with width  $L$  (the upper limit of the distance of the step advance) by one monolayer via *step advance*;  $t_{nuc}$  denotes the time to form one nucleus on the same substrate terrace.

The boundary in the growth diagram between layer-by-layer or 3D island growth is given approximately from  $t_{layer} \sim t_{nuc}$  :

$$\frac{L^3 \sqrt{S_C} r N_0}{\nu} \left( \frac{\Delta\mu - S_C \Delta\sigma}{\pi \Delta\mu^2} kT \right)^{1/2} \exp \left( \frac{\varphi + (E_{des} - E_{sd})/2 - \frac{4\chi^2 S_C}{\Delta\mu - S_C \Delta\sigma}}{kT} \right) \sim 1 \quad (8).$$

As can be seen in Eq. (8), layer-by-layer growth can be achieved above a certain threshold  $\Delta\mu$  even with  $\Delta\sigma > 0$ . In addition, the step width  $L$  is also an important parameter to tune the growth modes.<sup>11</sup>

By considering all the above discussions, taking Eq. (4) and Eq. (8), using  $\Delta\mu$  and  $T$  as variables, we are able to construct a growth phase diagram, as shown in Fig. 6. For simplicity, a Kossel crystal (i.e. here a layer refers to a layer of unit cell instead of an atomic monolayer) has been considered here and we only consider the nearest neighbor interaction for the strength (or the bond energy)  $b$ . The parameters used are:  $L=300$  nm;  $\nu=10^{13}$  Hz;  $a=0.4$  nm;  $r=10^{22}$  cm<sup>-2</sup>s<sup>-1</sup>;  $E_{des} = 2b$ ;  $E_{sd} = b$ ;  $\chi = b/2$ ; and  $\varphi = 3b$ . The change of surface energy  $\Delta\sigma$  is assumed to be zero.

The boundary  $L_1$  (red online) corresponds to  $\Delta\mu = 0$ . Below  $L_1$  the growth is non-stoichiometric due to the inability of completing the thermo-chemical transition from the quasi-vapor phase to solid phase of the certain compound.<sup>29</sup> Above  $L_1$  the film can be grown with the right stoichiometry. Boundary  $L_2$  is calculated using Eq.8 which separates the layer-by-layer growth from the 3D growth. Boundary  $L_3$  is calculated using Eq.4 which separates the poorly crystallized (P-C) and well crystallized (W-C) growth modes. Here we assume that all the boundaries are independent with each other. Thus, five different regions can be defined in the phase diagrams: non-stoichiometric; poorly crystallized 3D (P-C 3D); poorly crystallized

layer-by-layer (P-C LBL); well crystallized layer-by-layer (W-C LBL); well crystallized 3D (W-C 3D).

We note that the low laser repetition rate used (1 Hz) allows us to use steady-state considerations since the adatoms reach steady-state concentration during pulse intervals.<sup>28</sup> For simplification, we used the average deposition rate to analyze the process of *nucleation* and *step advance*. We also neglected the effect of epitaxial strain which affects step bunching phenomena in the step flow regime.<sup>11</sup>

## B. Comparison of Experimental Results with the Growth Diagram

It is important to verify whether the predicted phase diagram is consistent with the experimental data, and provides useful guidance on thin film growth of complex oxides by PLD.

The supersaturation, though not a direct tunable experimental parameter, is dependent on the temperature  $T$ , background oxygen pressure  $P$ , and the laser fluence (i.e. atom arrival rate  $r$ ).

For the dependence of  $\Delta\mu$  on the oxygen background pressure, we consider the vapor-solid phase transition (See supplementary material).  $\Delta\mu$  increases logarithmically with  $P$ :

$$\partial\Delta\mu(P, T) / \partial \ln P = RT \quad (9).$$

Similarly, the dependence of  $\Delta\mu$  on the arrival rate of material ablated from the target, which is proportional to the concentration of adatoms is:

$$\partial\Delta\mu(P, T) / \partial \ln r = RT \quad (10).$$

When the oxygen pressure and arrival rate are constant, one can derive the temperature dependence of the  $\Delta\mu$  (See supplementary material):

$$\partial\Delta\mu(P, T) / \partial \ln T \approx -\Delta h \quad (11)$$

where  $\Delta h$  denotes the molar enthalpy change between the solid and vapor phase.

In Fig. 7, we summarize our experimental AFM images and fit them into the theoretical growth diagram. For guiding purpose, we use different arrows to illustrate the qualitative dependence of growth mode under different growth parameters.

First, the temperature dependence of samples grown at a laser fluence of  $1 \text{ J/cm}^2$  is shown (the dash-dot-dot arrow). As discussed, the sample grown at  $720^\circ\text{C}$  has a poorly crystallized layer-by-layer feature, so it falls into P-C LBL region. By increasing the temperature to  $776^\circ\text{C}$ , the growth mode becomes three dimensional, corresponding to region P-C 3D; while further increasing the growth temperature to  $840^\circ\text{C}$  will lead the system to non-stoichiometry. Next, we study the temperature dependence of samples grown at relatively large laser fluence of  $4 \text{ J/cm}^2$ , as indicated by the dash-dot arrow. For sample grown at  $660^\circ\text{C}$ , the high supersaturation is able to put the system into a well crystallized layer-by-layer growth (region W-C LBL). By increasing the temperature from  $660^\circ\text{C}$  to  $760^\circ\text{C}$ , the sample crosses into a well crystallized 3D growth mode (region W-C 3D), consistent with our theoretical understanding.

We also examine the effect of laser fluence at fixed temperature and background pressure. Higher laser fluence translates into a higher ablated atom arrival rate, which implies a larger supersaturation. Indeed our experiments reveal that a higher laser fluence can lead the samples from a poorly-crystallized 3D phase (region P-C 3D) into a well-crystallized layer-by-layer phase (region W-C LBL), as indicated by long dash arrow in Fig. 7. Similar results have been revealed in experiments in which films become smoother when increasing the laser repetition rate.<sup>30,31</sup> The increase of the oxygen pressure also corresponds to an enhancement of the

supersaturation, which leads the thin film from a P-C 3D state to a P-C LBL state (solid arrow).

The experimental and theoretical results in this work are consistent with the findings of Metev et al.<sup>1,27</sup> in which a high deposition rate (high supersaturation) and a low growth temperature favored a 2D growth mode. The dependence of the boundary between step-flow growth and 2D island formation constructed by W. Hong et al.<sup>11</sup> on the atomic flux (supersaturation) differ from the findings of this work. On the other hand, the boundary constructed by W. Hong et al.<sup>11</sup> has not been verified by experiments. The observation of Ohtomo and Hwang<sup>12</sup> also fits nicely in our more complete growth diagram because according to our theoretical model, the supersaturation decreases with temperature and increases with oxygen pressure.

## CONCLUSION

To summarize, we studied the surface morphology, crystallinity and stoichiometry of LSMO thin films on STO (001) substrates grown using PLD. Various growth modes and phases have been observed. Theoretical considerations establish a growth phase diagram which reveals the nature of different growth modes in terms of supersaturation and temperature under the following condition: 1) the change of surface energy  $\Delta\sigma$  is ignorable; 2) the *step advance* is in the diffusion region; 3) the early stage of forming a layer is the most important in the growth process. As a result of the thorough theoretical framework, our derived growth diagram excellently matches the experimentally observed growth modes. As a case study, our results demonstrate the possibility of more comprehensive understanding on controlling growth process and film qualities in PLD growth.



\*Correspondence to: xiaoshan.xu@gatech.edu and [shenj5494@fudan.edu.cn](mailto:shenj5494@fudan.edu.cn)

## **ACKNOWLEDGMENTS**

Research supported by the US Department of Energy, Basic Energy Sciences, Materials Sciences and Engineering Division (P.C.S., T.Z.W., X.S.X.) and performed in part at the Center for Nanophase Materials Sciences (CNMS) (Z.G., I.K.) User Facility, which are sponsored at Oak Ridge National Laboratory by the Office of Basic Energy Sciences, US Department of Energy. We also acknowledge partial funding supports from the National Basic Research Program of China (973 Program) under Grant No. 2011CB921801 (J.S.), and the US DOE Office of Basic Energy Sciences, the US DOE Grant No. DE-SC0002136 (H.W.G., W.B.W)

## REFERENCES:

- <sup>1</sup> D.B. Chrisey and G.K. Hubler, *Pulse Laser Deposition of Thin Films* (1994).
- <sup>2</sup> H.M.C. and G. Eres, *Journal of Physics: Condensed Matter* **20**, 264005 (2008).
- <sup>3</sup> A. Ohtomo and H.Y. Hwang, *Nature* **427**, 423-426 (2004).
- <sup>4</sup> D.P. Norton, *Materials Science and Engineering: R: Reports* **43**, 139-247 (2004).
- <sup>5</sup> H.W. Jang, D.A. Felker, C.W. Bark, Y. Wang, M.K. Niranjan, C.T. Nelson, Y. Zhang, D. Su, C.M. Folkman, S.H. Baek, S. Lee, K. Janicka, Y. Zhu, X.Q. Pan, D.D. Fong, E.Y. Tsymbal, M.S. Rzchowski, and C.B. Eom, *Science* **331**, 886-889 (2011).
- <sup>6</sup> T.J. Jackson and S.B. Palmer, *Journal of Physics D: Applied Physics* **27**, 1581 (1994).
- <sup>7</sup> P.R. Willmott and J.R. Huber, *Rev. Mod. Phys.* **72**, 315-328 (2000).
- <sup>8</sup> P.R. Willmott, *Progress in Surface Science* **76**, 163-217 (2004).
- <sup>9</sup> M.N.R. Ashfold, F. Claeysens, G.M. Fuge, and S.J. Henley, *Chemical Society Reviews* **33**, 23-31 (2004).
- <sup>10</sup> I.V. Markov, *Crystal Growth for Beginners: Fundamentals of Nucleation, Crystal Growth and Epitaxy*, 2nd ed. (2003).

- <sup>11</sup> W. Hong, H.N. Lee, M. Yoon, H.M. Christen, D.H. Lowndes, Z. Suo, and Z. Zhang, *Physical Review Letters* **95**, 95501 (2005).
- <sup>12</sup> A. Ohtomo and H.Y. Hwang, *Journal of Applied Physics* **102**, 83704 (2007).
- <sup>13</sup> S.K. Sinha, R. Bhattacharya, S.K. Ray, and I. Manna, *Materials Letters* **65**, 146-149 (2011).
- <sup>14</sup> D. Sun, L. Yin, C. Sun, H. Guo, Z. Gai, X.-G. Zhang, T.Z. Ward, Z. Cheng, and J. Shen, *Physical Review Letters* **104**, 236602 (2010).
- <sup>15</sup> S. Brivio, C. Magen, A.A. Sidorenko, D. Petti, M. Cantoni, M. Finazzi, F. Ciccacci, R. De Renzi, M. Varela, S. Picozzi, and R. Bertacco, *Physical Review B* **81**, 94410 (2010).
- <sup>16</sup> X. Hong, A. Posadas, A. Lin, and C.H. Ahn, *Physical Review B* **68**, 134415 (2003).
- <sup>17</sup> J.D. Ferguson, Y. Kim, L.F. Kourkoutis, A. Vodnick, A.R. Woll, D.A. Muller, and J.D. Brock, *Advanced Materials* **23**, 1226-1230 (2011).
- <sup>18</sup> F. Tsui, M.C. Smoak, T.K. Nath, and C.B. Eom, *Applied Physics Letters* **76**, 2421-2423 (2000).
- <sup>19</sup> H.-Y. Zhai, J.X. Ma, D.T. Gillaspie, X.G. Zhang, T.Z. Ward, E.W. Plummer, and J. Shen, *Physical Review Letters* **97**, 167201 (2006).
- <sup>20</sup> T.Z. Ward, S. Liang, K. Fuchigami, L.F. Yin, E. Dagotto, E.W. Plummer, and J. Shen, *Physical Review Letters* **100**, 247204 (2008).

- <sup>21</sup> *X-Ray Data Booklet* (Lawrence Berkeley National Laboratory, 2009).
- <sup>22</sup> <http://www.veeco.com/pdfs/mbe/vapor-pressure-Chart-1.pdf>.
- <sup>23</sup> I. Ohkubo, H.M. Christen, S.V. Kalinin, J. G. E. Jellison, C.M. Rouleau, and D.H. Lowndes, *Applied Physics Letters* **84**, 1350-1352 (2004).
- <sup>24</sup> M. Volmer and A. Weber, *Zeitschrift Für Physikalische Chemie* **119**, 277 (1926).
- <sup>25</sup> F.C. Frank and J.H. van der Merwe, *Proceedings of the Royal Society of London. Series A. Mathematical and Physical Sciences* **198**, 205-216 (1949).
- <sup>26</sup> I. Stranski and L. Krastanov, *Sitzungsber. Akad. Wissenschaft Wien* **146**, 797 (1938).
- <sup>27</sup> S. Metev and K. Meteva, *Applied Surface Science* **43**, 402-408 (1989).
- <sup>28</sup> M. Kareev, S. Prosandeev, B. Gray, J. Liu, P. Ryan, A. Kareev, E.J. Moon, and J. Chakhalian, *Journal of Applied Physics* **109**, 114303 (2011).
- <sup>29</sup> W. Wang, Z. Gai, M. Chi, J.D. Fowlkes, J. Yi, L. Zhu, X. Cheng, D.J. Keavney, P.C. Snijders, T.Z. Ward, J. Shen, and X. Xu, *Phys. Rev. B* **85**, 155411 (2012).
- <sup>30</sup> G.H. Lee, B.C. Shin, and B.H. Min, *Materials Science and Engineering: B* **95**, 137-140 (2002).
- <sup>31</sup> J. Shin, S.V. Kalinin, A.Y. Borisevich, E.W. Plummer, and A.P. Baddorf, *Applied Physics Letters* **91**, 202901 (2007).



**Figure Captions:**

FIG. 1. (Color online) (a) AFM image (left) and RHEED image (right) of SrTiO<sub>3</sub> (001) substrate. (b), (c) AFM, real-time RHEED oscillations and RHEED images of samples grown at 720 °C and 776 °C under 1J/cm<sup>2</sup> laser fluence. (d) AFM (upper left) and SEM (upper right) images of sample grown at 840 °C under 1J/cm<sup>2</sup> laser fluence. Mn (lower left) and O (lower right) EDX spectroscopy are shown corresponding to SEM image area.

FIG. 2. (Color online) Samples grown at different temperatures with laser fluence of 4J/cm<sup>2</sup>. (a), (b) surface morphologies of samples grown at 660 °C and 760 °C. (c), (d) corresponding RHEED oscillations and image of sample in (b).

FIG. 3. (Color online) (a) growth pressure dependence of surface morphology under growth temperature of 730 °C and laser fluence of 1J/cm<sup>2</sup>. (b) surface roughness (in unit of nm) map of the sample under oxygen pressure gradient. The dashed arrow indicates the direction of increasing local pressure.

FIG. 4. (Color online) Laser fluence dependence of samples grown at (a) 1J/cm<sup>2</sup> and (b) 2.2J/cm<sup>2</sup>, both under growth temperature of 740 °C. (c), (d) corresponding RHEED oscillations and image of the sample in (b).

FIG. 5. (Color online) Microscopic illustration of the growth processes. (a) Schematic diagram of

the atomic process in the deposition. (b) Schematic of the poor crystalization (left) and the good crystalization (right). (c) Schematic of the 2D layer-by-layer growth and the 3D growth.

FIG. 6. (Color online) The theoretically constructed growth diagram.  $L_1$  (red): boundary between stoichiometric and non-stoichiometric growth;  $L_2$  (green): boundary between layer-by-layer (LBL) and 3D growth;  $L_3$  (blue): boundary between the poorly crystallized (P-C) and well crystallized (W-C) growth.

FIG. 7. (Color online) Qualitative comparison between experimental results and theoretical growth diagram. Arrows description: dash-dot-dot: temperature increase ( $720\text{ }^\circ\text{C}$ ,  $776\text{ }^\circ\text{C}$ ,  $840\text{ }^\circ\text{C}$ ) under constant laser fluence ( $1\text{J}/\text{cm}^2$ ) and pressure; dash-dot: temperature increase ( $660\text{ }^\circ\text{C}$ ,  $760\text{ }^\circ\text{C}$ ) under constant laser fluence ( $4\text{J}/\text{cm}^2$ ) and pressure; long dash: laser fluence increase ( $1\text{J}/\text{cm}^2$ ,  $2.2\text{ J}/\text{cm}^2$ ) under constant temperature and pressure; solid: pressure increase under constant temperature ( $730\text{ }^\circ\text{C}$ ) and laser fluence ( $1\text{J}/\text{cm}^2$ ).

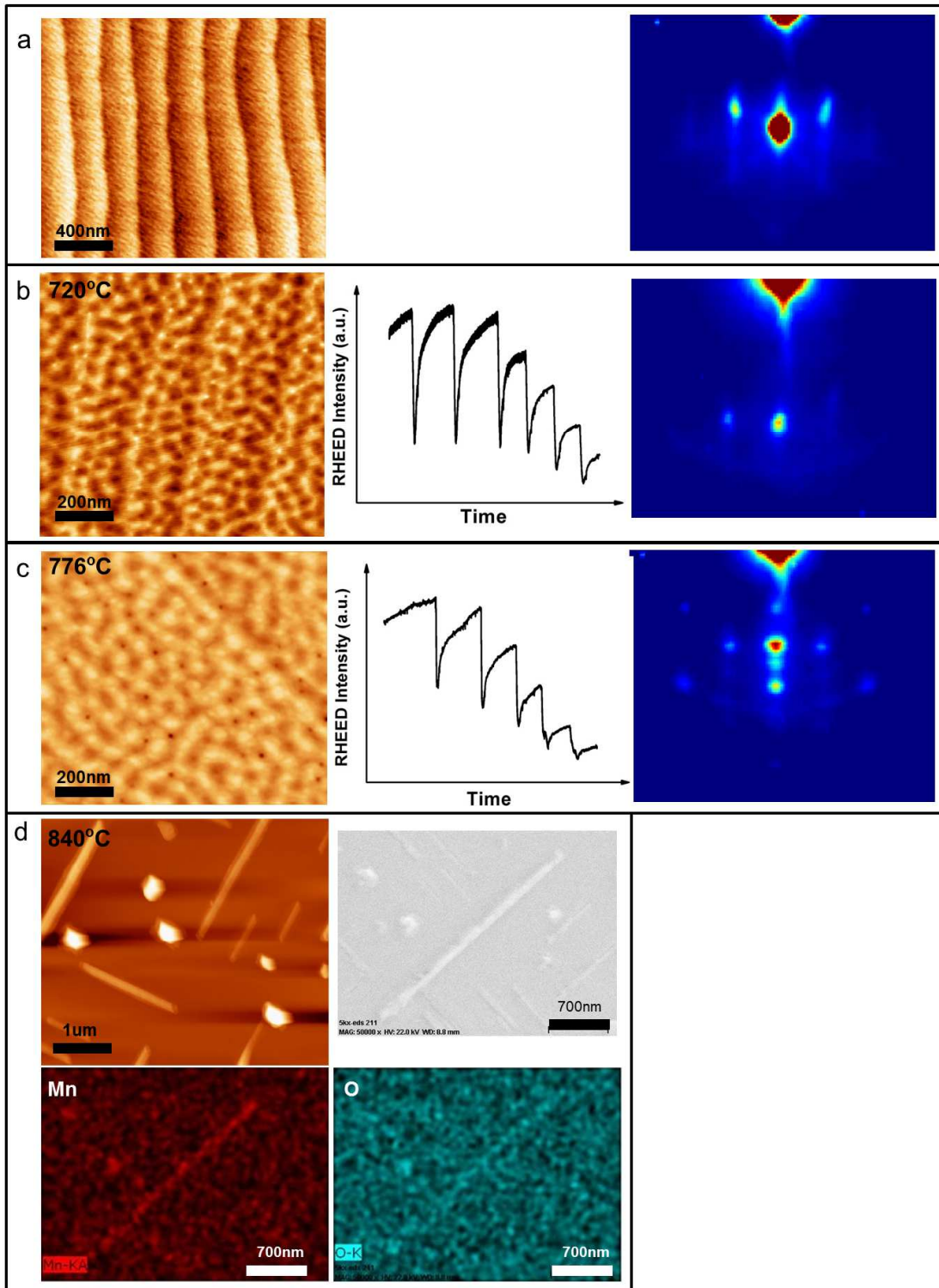


Figure 1.

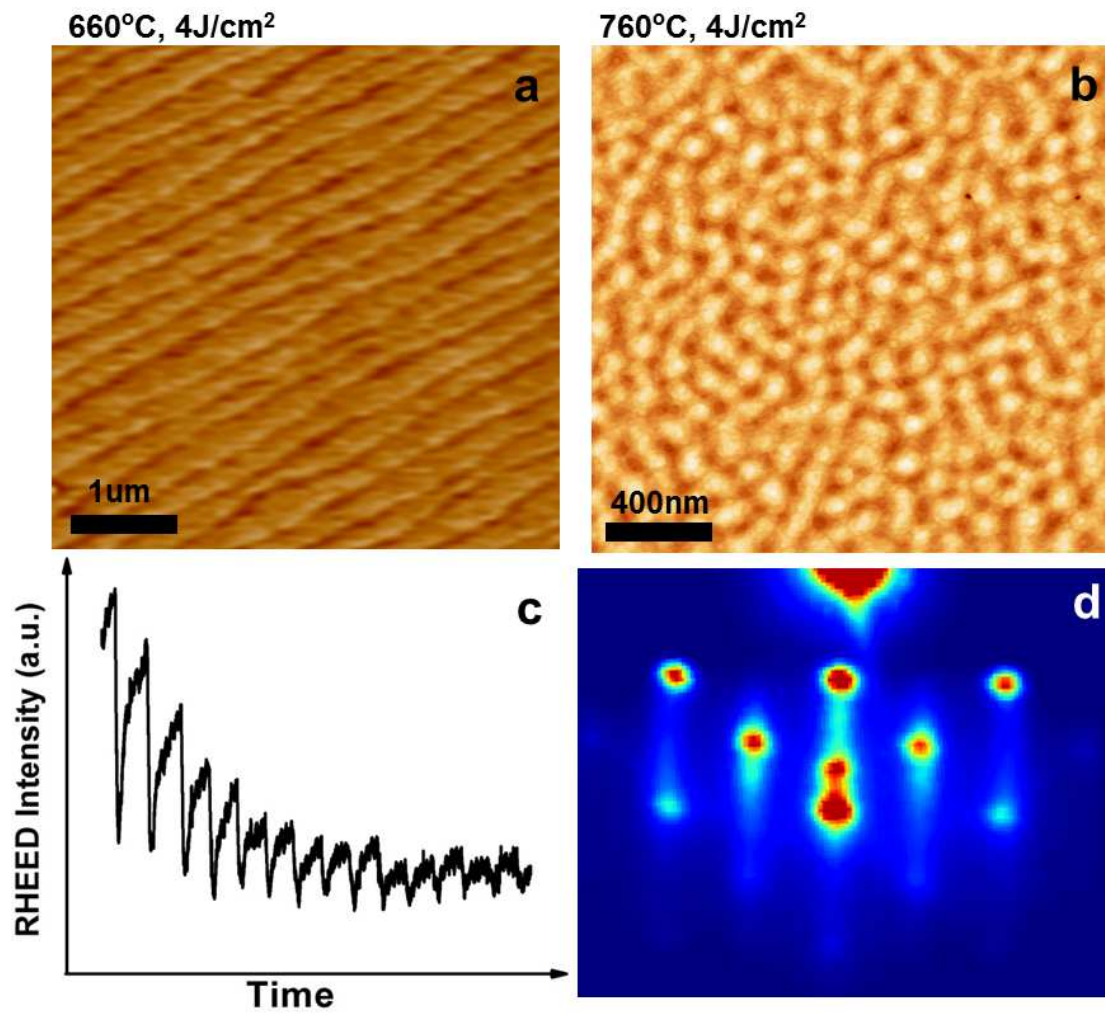


Figure 2.

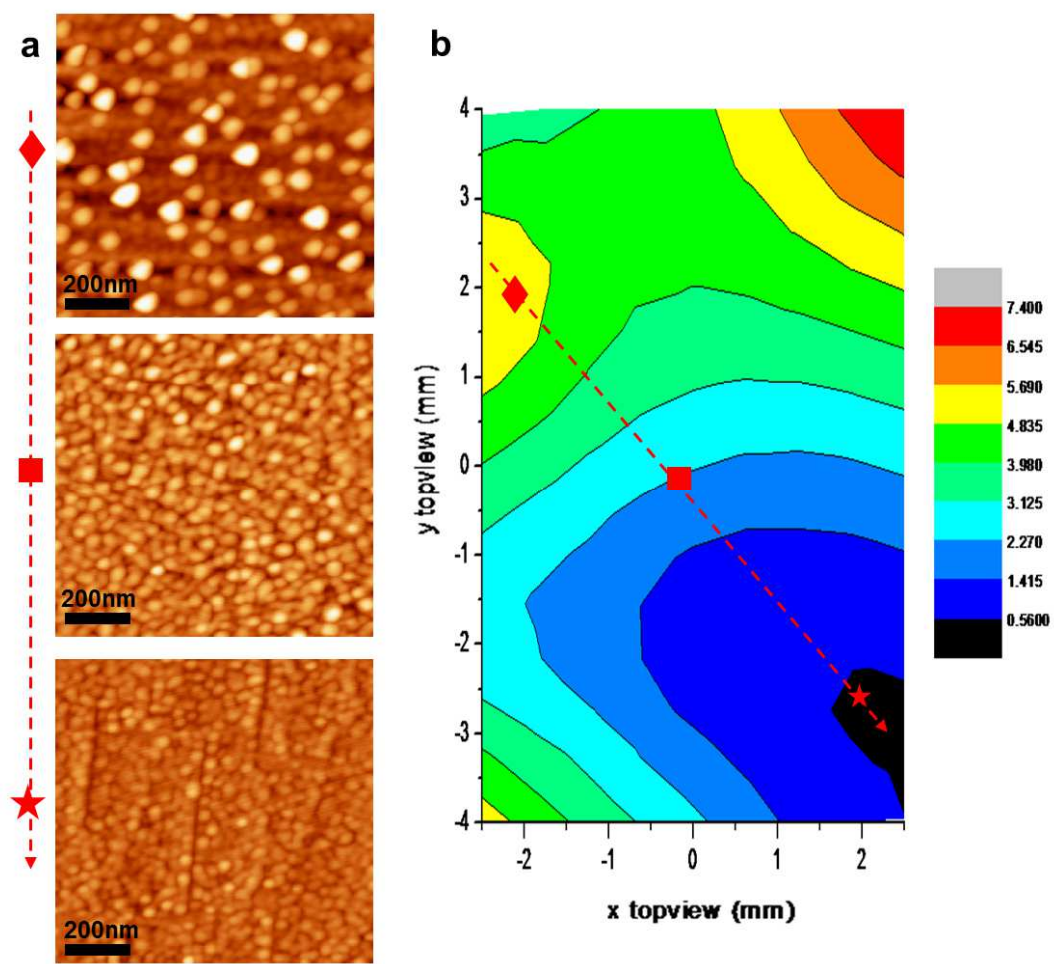


Figure 3.

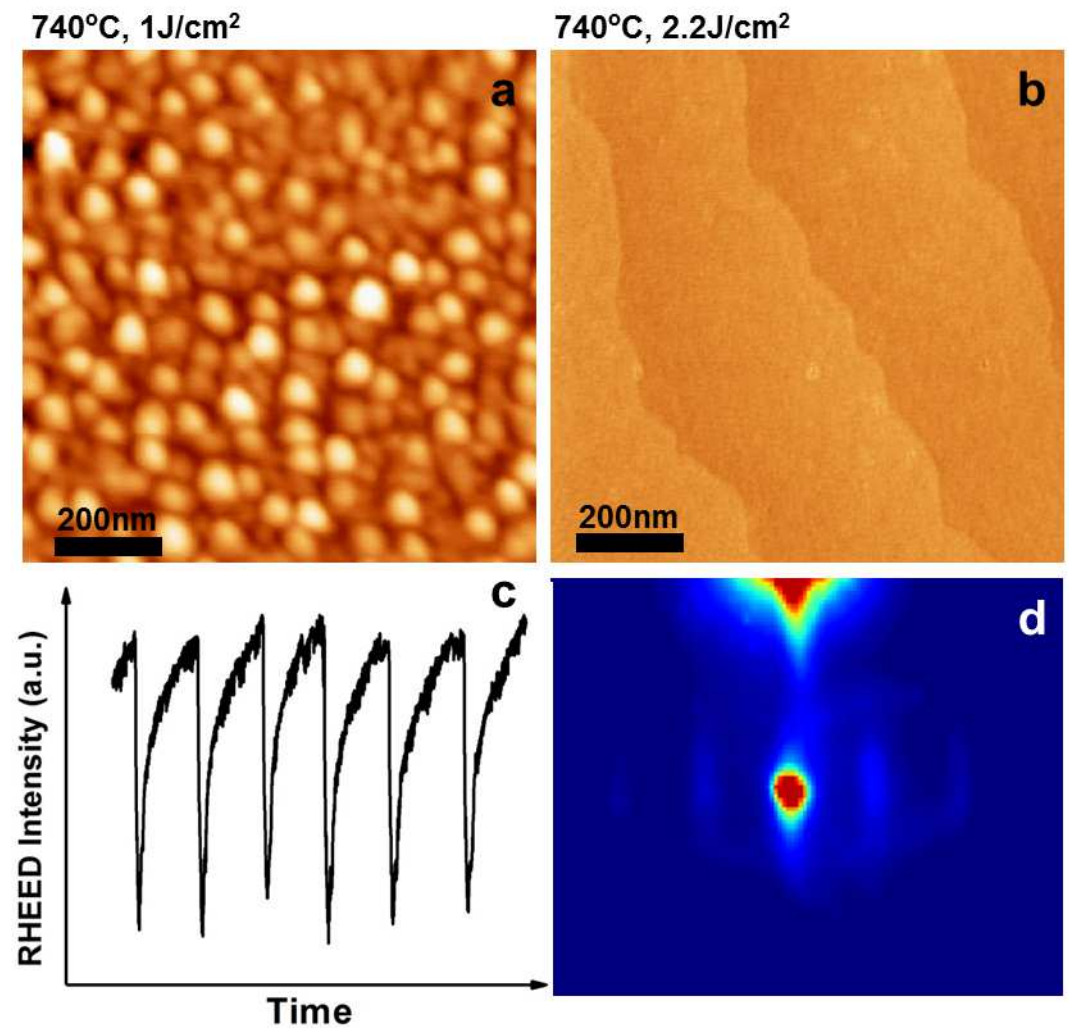


Figure 4.

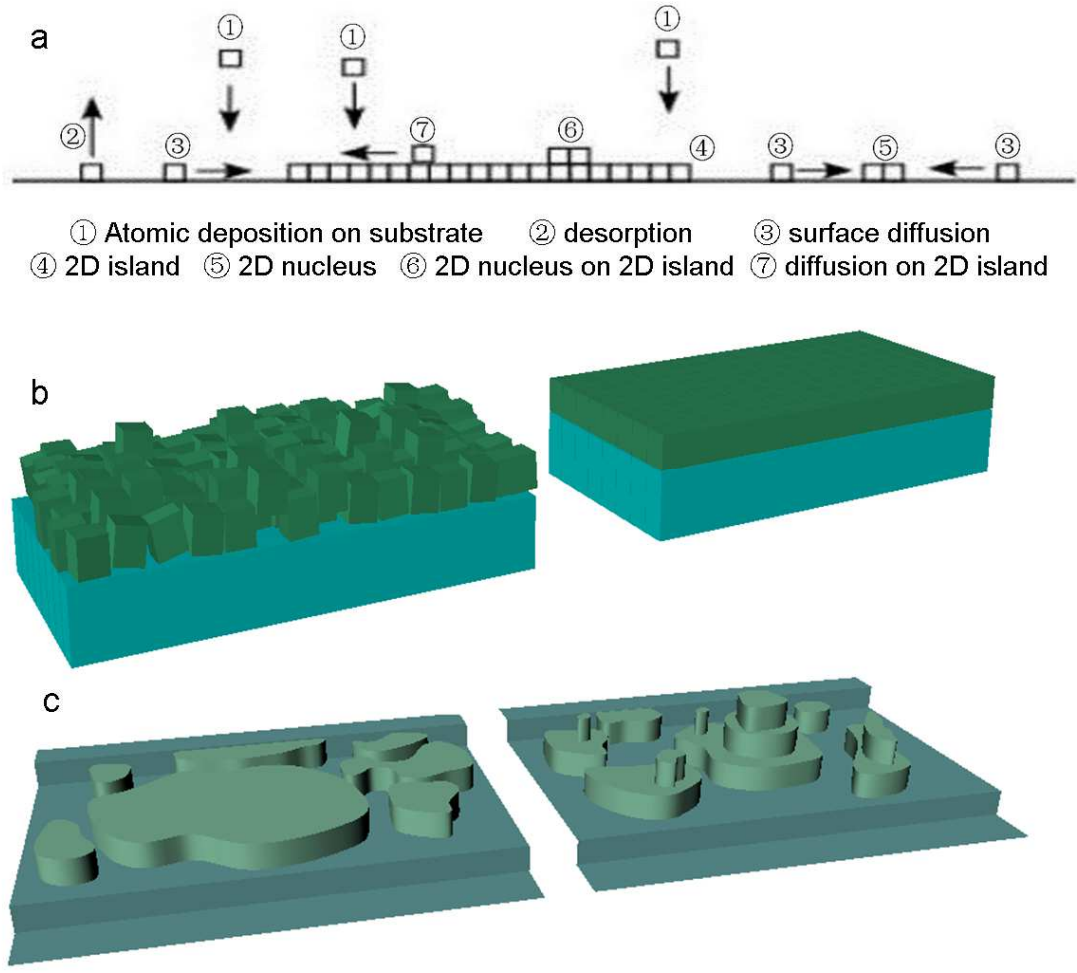


Figure 5.

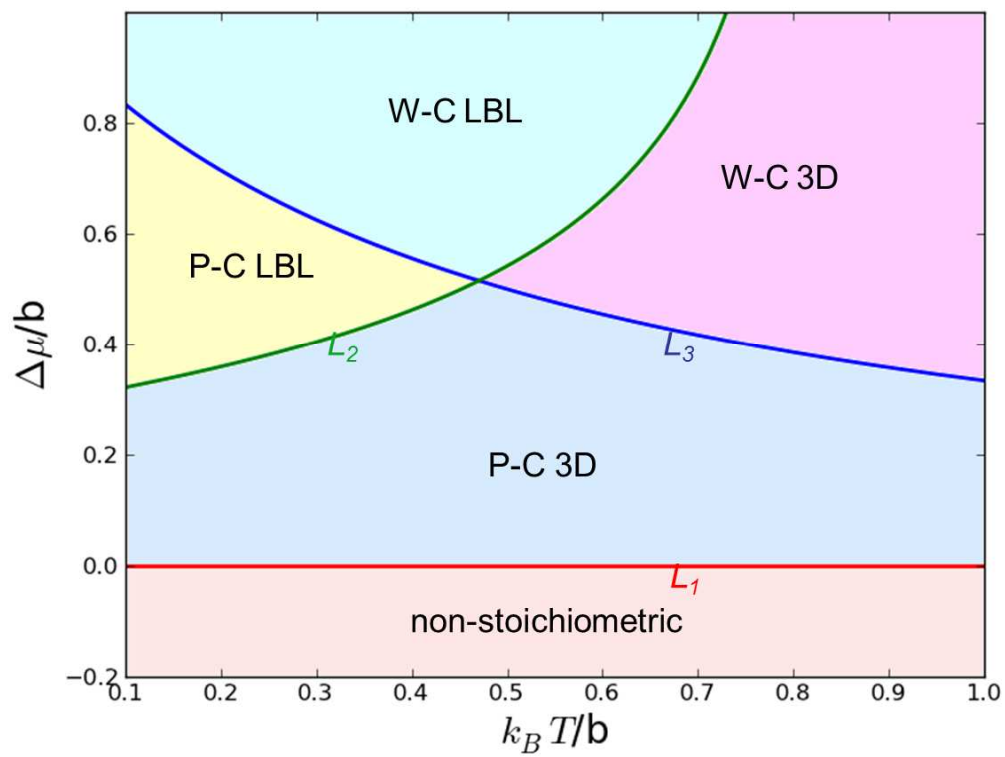


Figure 6.

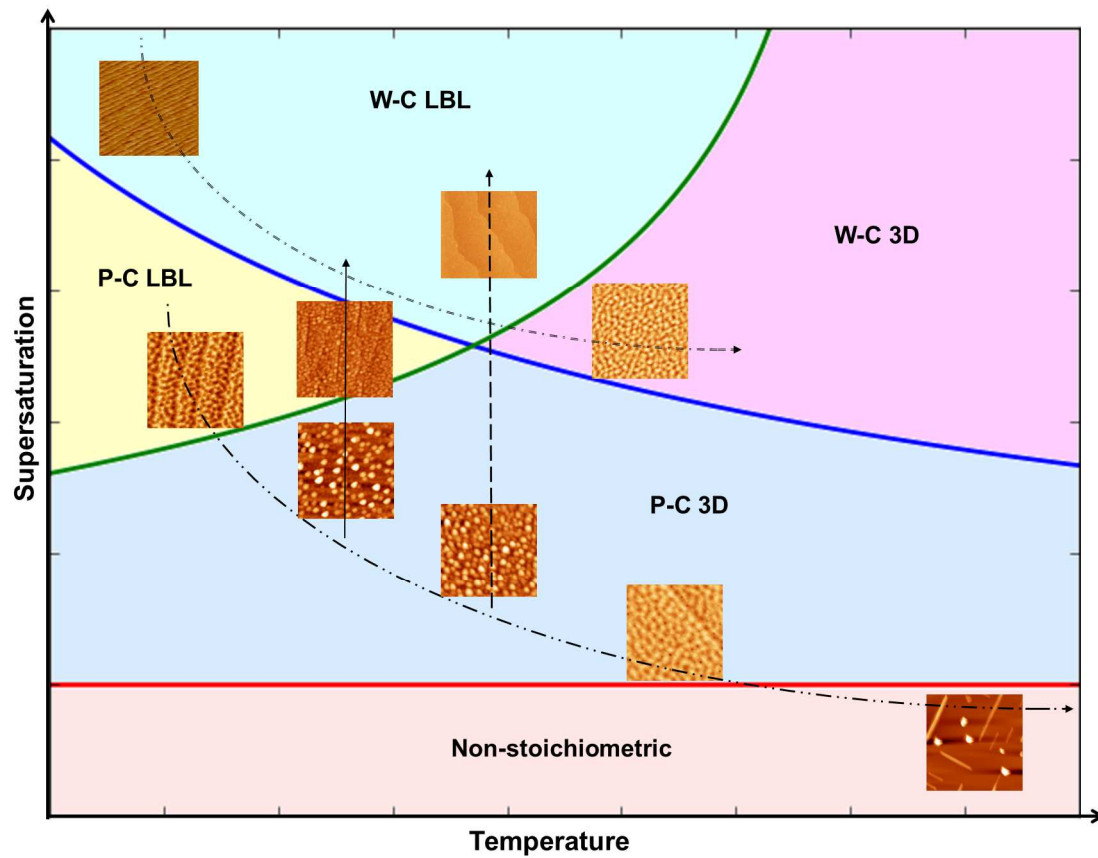


Figure 7.

	Counts of film	Counts of film and rod	Counts of rod	Standard Relative Intensity	Counts of rod normalized with standard intensity
<b>Mn (K<math>\alpha</math>)</b>	52	120	68 $\pm$ 9	150	0.45 $\pm$ 0.06
<b>O (K)</b>	470	529	59 $\pm$ 22	151	0.39 $\pm$ 0.14

**Table 1.** EDX analysis of non-stoichiometric sample (840 °C, 1J/cm<sup>2</sup>).

## Supplementary material

### A: Nucleation

To form small nucleus on top of a surface, the chemical potential of the vapor phase has to overcome a barrier due to the fact that the small nuclei have higher energy per atom than their bulk counterpart. For 2D nucleation: the change of the Gibbs free energy for forming such a square nucleus is

$$\Delta G = -\frac{l^2}{S_c} \Delta\mu + l^2 \Delta\sigma + 4l\chi$$

$$\Delta\sigma = \sigma + \sigma_i - \sigma_s$$

where  $l$  is the length of the nucleus,  $S_c$  is the area of the unit cell,  $\sigma$  is the surface energy of the 2D nucleus,  $\sigma_i$  is the interface energy between the nucleus and the underlying layer and  $\sigma_s$  is the surface energy underneath the nucleus and  $\chi$  is the edge energy per unit length.

The maximum value of  $\Delta G$  with respect to the length  $l$  is the barrier:

$$\Delta G^* = \frac{4\chi^2 s_c}{\Delta\mu - s_c \Delta\sigma}$$

Correspondingly, the critical length for the maximum  $\Delta G$  is

$$l^* = \frac{2\chi s_c}{\Delta\mu - s_c \Delta\sigma}$$

The nuclei smaller than this size will decay and those larger than this size will grow.

Because of this barrier, and the dependence on the number of adatoms and their diffusion length, the speed of 2D nucleation takes the form:

$$J_{nuc} = f(\Delta\mu) \Gamma^{-1/2} \exp\left(\frac{-H(\Delta\mu)}{kT}\right)$$

$$f(\Delta\mu) = 2\sqrt{s_c} aRN_0 \left(\frac{\Delta\mu - s_c \Delta\sigma}{\pi k}\right)^{1/2}$$

$$H(\Delta\mu) = \frac{4\chi^2 s_c}{\Delta\mu - s_c \Delta\sigma} - (E_{des} - E_{sd})$$

which is the Eq. (1-3) in the main text.

## B: Diffusion and Step advance

Fig. 1(a) in the main text depicts the atomic process during the pulsed laser deposition. The density of atoms adsorbed on the surface  $n_{ad}$  (mostly the case 3 in Fig. 5(a)) is proportional to the atom arrival rate  $r$  and the adsorption time of the atoms. Therefore,

$$n_{ad} \propto r\tau_{ad}$$

given that the sticking coefficient is unity, which is the case for high energy incoming atomic flux.

The life time of the adatoms  $\tau_{ad}$  is the time between the adsorption and the desorption which involves overcoming an energy barrier  $E_{des}$ , as shown in Fig. S1. Therefore

$$\tau_{ad} = \frac{1}{\nu} \exp\left(\frac{E_{des}}{kT}\right)$$

where  $\nu$  is the vibrational frequency of the adatom.

During the lifetime of an adatom, it moves along the surface according to the thermal fluctuation, or random walk, i.e. diffusion. The diffusion coefficient is

$$D_{sd} = a^2 \nu \exp\left(-\frac{E_{sd}}{kT}\right)$$

where  $a$  is the lattice constant and  $E_{sd}$  is the diffusion energy barrier (Fig. S1). Therefore the diffusion length is given as

$$L_{sd} = \sqrt{D_{sd} \tau_{ad}} = a \exp\left(\frac{E_{des} - E_{sd}}{2kT}\right)$$

The speed of step advance involves two processes. First, an adatom moves to a step kink by diffusion, the rate is described as the mean distance  $L_{sd}$  divided by the mean residence time  $\tau_{ad}$

$$V_d = \frac{L_{sd}}{\tau_{ad}} = a \nu \exp\left(-\frac{E_{des} + E_{sd}}{2kT}\right)$$

Second, the adatoms overcome an energy barrier to attach to the step kink (Fig. S1), the rate of which can be described as

$$V_{sk} = \frac{a^2 \nu}{\delta_0} \exp\left(-\frac{U}{kT}\right)$$

where  $\delta_0$  is the mean distance between step kinks and  $U$  is the energy barrier for adatom to attach on a step kink. Because in most cases  $E_{des} + E_{sd} \gg U$ , the rate of step advance is limited by the diffusion process.

Therefore, the speed of step advance takes the form:

$$V_{sa} = 2a \nu \frac{\Delta\mu}{kT} \exp\left(-\frac{\varphi - (E_{des} - E_{sd})/2}{kT}\right)$$

which is the Eq. (5) in the main text.

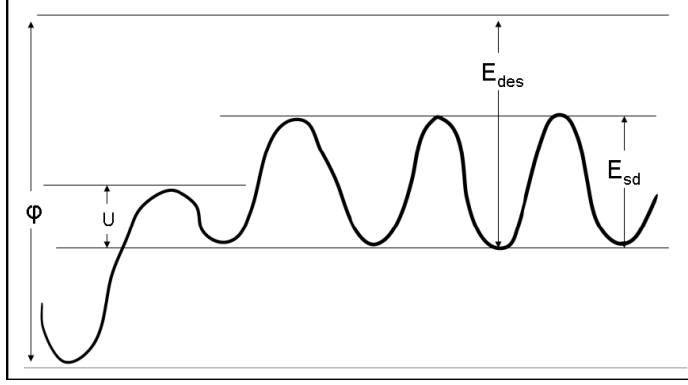


FIG. S1.: Energy potential plot.  $\phi$  : energy potential for kink position;  $E_{des}$  : desorption energy;  $E_{sd}$  : surface diffusion potential;  $U$ : energy barrier for attaching to kink position.

### C: Thermodynamics of phase transition

As seen in Fig. S2, in gas-solid phase transition, the phase boundary as a function of  $P(T)$  divides the two phases. In equilibrium, if the  $(P, T)$  combination falls on the solid side the system is in its solid phase. On the other hand, at non-equilibrium, for a finite amount of time, a system can be with a  $(P, T)$  combination on the solid side but still remains in gas phase. This chemical potential difference between the combination  $(P, T)$  in solid phase the combination  $(P_0, T)$  on phase boundary is called supersaturation.

The quantitative definition of supersaturation for point  $(P, T)$  is

$$\Delta\mu = RT \ln\left(\frac{P}{P_0}\right)$$

where  $P_0$  is the pressure value at the equilibrium state. Same analogy holds for the atom arrival rate. Thus, supersaturation increases with increasing pressure and laser energy.

To find the dependence of supersaturation on temperature, one has to consider the

supersaturation change at the phase boundary, as shown in Fig. S2:

$$\begin{aligned}\Delta\mu(P, T_2) - \Delta\mu(P, T_1) &= [\mu(P, T_2) - \mu(P_b, T_2)] - [\mu(P, T_1) - \mu(P_a, T_1)] \\ &= [\mu(P, T_2) - \mu(P, T_1)] - [\mu(P_b, T_2) - \mu(P_a, T_1)]\end{aligned}$$

From Gibbs-Duham equation  $d\mu = vdP - sdT$  where  $S$  denotes the entropy, the first term:

$$[\mu(P, T_2) - \mu(P, T_1)] = -s(T_2 - T_1)$$

The second term is the chemical potential changes along the phase boundary, which has the relation  $d \ln P = -\Delta h / R d(1/T)$ , where  $\Delta h$  is the enthalpy change between crystal and vapor phase per mole, which does not vary too much with temperature.

Using Gibbs-Duham equation again, one can get:

$$d\Delta\mu = -\Delta h d(\ln T) + [s(P, T) - s(P, \text{boundary})]dT, \text{ where } s(P, \text{boundary}) \text{ is the entropy at the phase boundary with pressure } P. \text{ Since entropy does not change very much within the solid phase, } d\Delta\mu \approx -\Delta h d(\ln T).$$

One can see that at constant pressure, the supersaturation decreases approximately exponentially with increasing temperature.

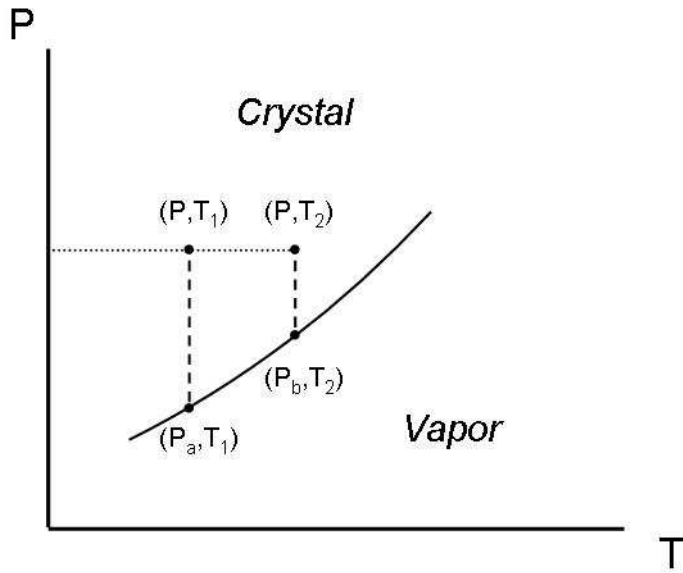


FIG. S2. Illustration of solid-gas phase diagram

#### **D: Features of poorly and well crystallized growth**

As shown in Fig. S3, XRD rocking curves corresponding to different surface morphologies are present to demonstrate the crystallization properties for sample grown at 740 °C under laser fluence of 1J/cm<sup>2</sup> and 2.2J/cm<sup>2</sup>.

Here, we present another experimental distinction of multilayer poorly-crystallized and multilayer well-crystallized features of the thin film sample in use of post-annealing process.

As shown in Fig. S4, a poorly crystallized surface is obtained as-grown. After annealing the sample in O<sub>2</sub> at 700 °C for 3 hours, a much more flat and well-crystallized film is achieved.

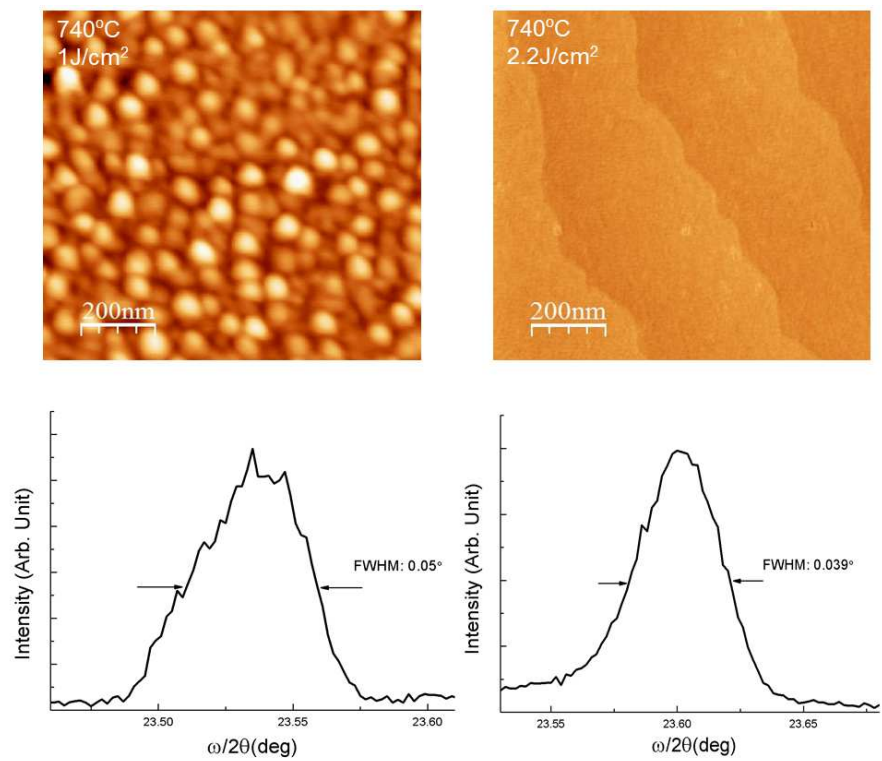


FIG. S3. AFM images and their corresponding rocking curve of (002) peak.

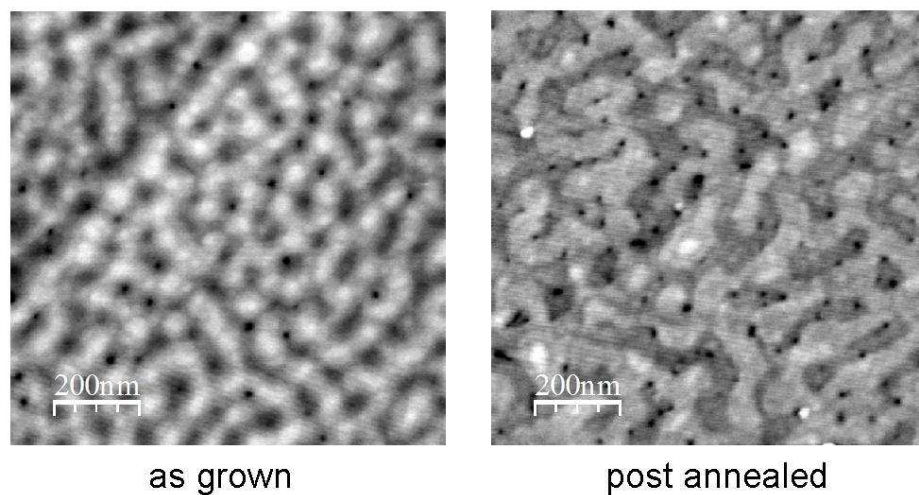


FIG. S4. comparison on surface morphologies of as-grown sample (left) and the same sample annealed in O<sub>2</sub> at 700 °C (right).